

## A THREE-DIMENSIONAL MAP OF TITAN'S TROPOSPHERIC HAZE DISTRIBUTION BASED ON HUBBLE SPACE TELESCOPE IMAGING<sup>1</sup>

ELIOT F. YOUNG

Southwest Research Institute, Suite 429, 1050 Walnut Street, Boulder, CO 80302

PASCAL RANNOU

Service d'Aéronomie, CNRS, 4 place Jussieu, F-75252 Paris, France

CHRISTOPHER P. MCKAY

NASA Ames Research Center, Moffet Field, CA 94035

CAITLIN A. GRIFFITH<sup>2</sup>

Department of Physics and Astronomy, Northern Arizona University, Flagstaff, AZ 86011-6010

AND

KEITH NOLL

Space Telescope Science Institute, 3700 San Martin Drive, Baltimore, MD 21218

Received 2000 December 4; accepted 2002 January 18

### ABSTRACT

We use *Hubble Space Telescope* (*HST*) images of Titan obtained in late 1996 to determine a three-dimensional map of haze optical depth in Titan's atmosphere. These images, taken at six wavelengths from 888 to 953 nm, probe Titan's atmosphere at various altitudes ranging from the surface to roughly 100 km. We solve for the total haze optical depths that best match each *HST* image and then combine the results from each wavelength into a composite three-dimensional map. The total optical depths due to haze in these maps range from 1.7 in the northernmost latitudes to 2.9 in the southernmost ones. The vertical haze profiles are roughly exponential except for a gap between 20 and 40 km, which may be a result of ethane or methane condensation onto tholins. There is a concentration of haze in the northernmost latitudes between 0 and 15 km above the surface.

*Key words:* planets and satellites: individual (Titan)

### 1. INTRODUCTION

The *Voyager* radio occultation experiments (Lindal et al. 1983) determined the vertical temperature and pressure profiles at two separate points on Titan's limb (Fig. 1). One of the more interesting questions arising from that experiment is whether methane or ethane clouds form below the temperature inversion that occurs at an altitude of 40 km. McKay et al. (1997) recount some of the evidence suggesting that methane is actually supersaturated in Titan's troposphere (the region below 40 km). They point out that the spectra returned from the IRIS instrument on the *Voyager* spacecraft indicate that the lower atmosphere is optically thicker at 300–500 cm<sup>-1</sup> than it would be if methane were simply saturated. Furthermore, Titan's observed thermal structure requires the extra opacity in the troposphere. Without it, Titan's greenhouse effect would be too weak to produce the observed surface temperatures. Finally, Titan's tropospheric lapse rate exceeds that of a moist adiabat, suggesting that tropospheric methane is not condensing onto grains in significant quantities. A recent development is a report by Griffith et al. (1998) on the discovery of clouds that exist in ephemeral storms, based on elevated albedos

that have been irregularly observed in certain spectral windows.

What are the characteristic size and distribution of aerosols in Titan's atmosphere? Rages & Pollack (1983) fitted vertical profiles of haze in the upper atmosphere above 100 km using high phase angle images (see Fig. 2) taken as *Voyager* flew by Titan's sunlit limb. Figure 3 (Fig. 5 in Rages & Pollack 1983) shows the vertical extinction profiles associated with the north polar hood and detached haze layer that are apparent in the *Voyager* images.

Titan's aerosols are dark at the *Voyager* Vidicon wavelengths (shortward of 600 nm) but extremely bright at longer wavelengths, resulting from a drop in the imaginary index of refraction for wavelengths longer than 700 nm. We see this directly from Titan images taken in different CCD wavelengths; images at 600 nm or shorter are *darker* where the haze is more abundant (currently the south pole), but those same regions are *brighter* when imaged at 800 or 900 nm. The imaginary indices of "Titan tholin" lab analogs are low between 0.6 and 5  $\mu$ m (Khare et al. 1984), consistent with the observed wavelength dependence of the north-south asymmetry.

Several papers in the early 1980s reported aerosol sizes ranging from 0.1 to 0.5  $\mu$ m (Tomasko 1980; Rages & Pollack 1980; Rages, Pollack, & Smith 1983). It was suspected at the time that the assumption of single-size spherical particles was responsible for the discrepancy. Recent attempts to fit *I/F* center-to-limb *Voyager* profiles assuming that the aerosols are fractal aggregates instead of spheres have been more successful (West & Smith 1991; Rannou et al. 1997), particularly when fitting the different data sets that had pre-

<sup>1</sup> Based on observations made with the NASA/ESA Hubble Space Telescope, obtained at the Space Telescope Institute, which is operated by the Association of Universities for Research in Astronomy, Inc., under NASA contract NAS 5-26555. These observations are associated with proposal 6733.

<sup>2</sup> Current address: Lunar and Planetary Laboratory, Department of Planetary Sciences, University of Arizona 1629 East University Boulevard, Tucson AZ 85721.

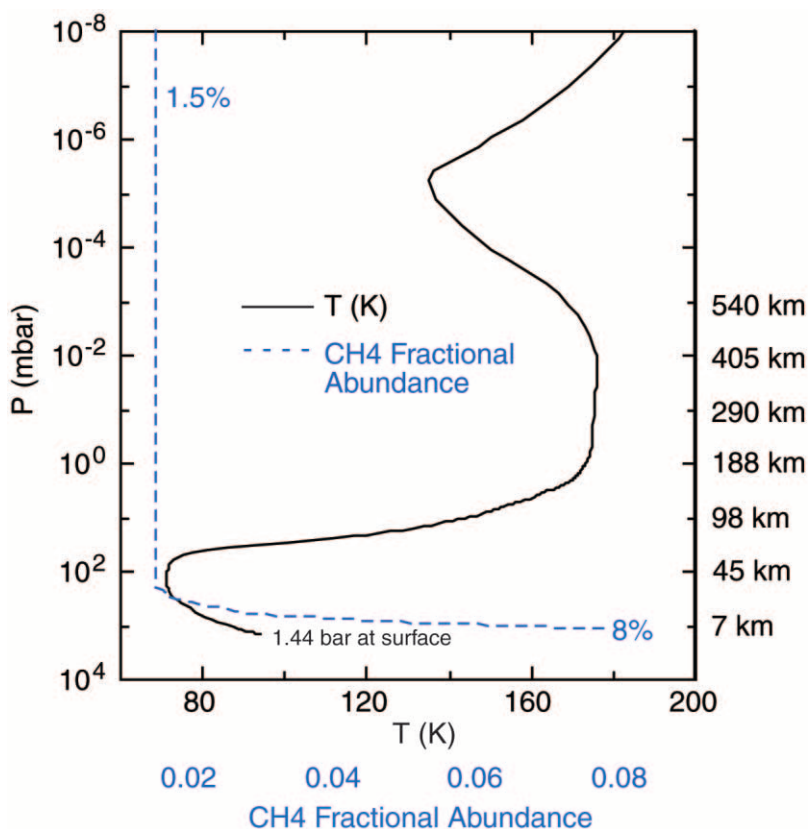


FIG. 1.—Titan's atmospheric profile, showing temperature and methane concentration as functions of altitude (Lellouch et al. 1989)

viously produced inconsistent size estimates. *Hubble Space Telescope* (*HST*) observations of Titan's shadow cast onto Saturn's disk in 1995 (Karkoschka & Lorenz 1997) suggest that the size of aerosols is a function of latitude as well as altitude. Given that Titan's haze distribution exhibits large north-south asymmetries, a latitudinal size dependence would not be surprising. Lorenz et al. (1999) summarize the evolution of the north-south asymmetry, which changes

sign every 16 years. The questions of haze (where is it produced and how is it transported) and clouds (whether they exist, and whether methane is supersaturated in Titan's troposphere) motivate our efforts to produce a three-dimensional map of haze opacity. We do not attempt to fit aerosol sizes in this paper; we use altitude-dependent haze scattering parameters derived by P. R. (see Fig. 6 below).

In this paper, we present Wide Field Planetary Camera 2 (WFPC2) images taken in six filters from 888 to 953 nm. Since methane's absorption coefficient varies by 3 orders of

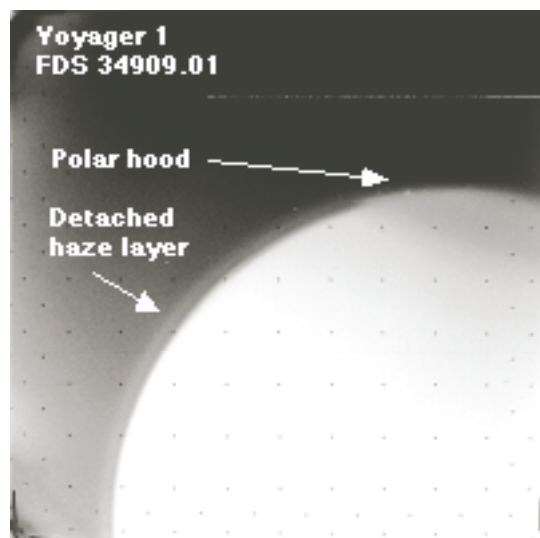


FIG. 2.—One of the *Voyager* images (circa 1980) showing a detached haze layer above a gap at roughly 300–350 km and a north polar hood. The hood represents a haze concentration. It is dark at *Voyager* Vidicon wavelengths, but it would be bright at wavelengths near  $1\ \mu\text{m}$ .

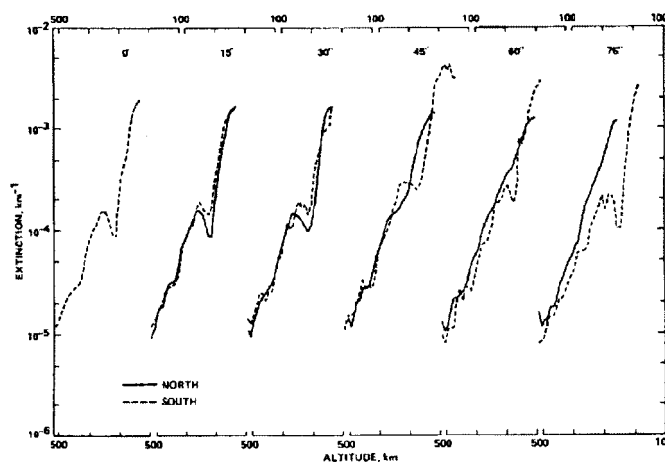


FIG. 3.—Aerosol extinction profiles presented by Rages & Pollack (1983) based on high spatial resolution *Voyager* images. The profiles are roughly exponential with scale heights that are close to that of the  $\text{N}_2$  number density profile, but the gap between 300 and 350 km is clearly visible. The Rages & Pollack haze profiles extend down to roughly 150 km.

magnitude across this filter set, methane acts as an effective vertical discriminator. We combine haze abundances determined from each individual filter into composite three-dimensional haze distributions by weighting the result from each filter by its relative importance at each altitude.

We present vertical haze profiles for Titan's disk at two rotational phases, with a linear spatial resolution of about 400 km. We find that the total one-way optical depths due to haze (based on the column method; § 3.4.1) range from 2.1 to 2.7, depending on latitude. The haze profile is only roughly exponential in the altitude ranges probed by the WFPC2 image set, with a gap around 16–40 km. We also find a local concentration of haze at northern latitudes just above the surface (0–16 km), in contrast to the monotonically decreasing south-to-north slope in haze abundance seen at higher altitudes.

## 2. OBSERVATIONS

All of the observations in this paper were taken with the WFPC2 instrument on *HST* as part of Cycle 6 program GO-6733. This program consisted of five identical visits to Titan spaced over a period of 16 days (Table 1). Four of the visits were separated by 4 days (to obtain views of Titan at 90° intervals), while a fifth was scheduled 24 hr after visit 2 to look for atmospheric phenomena that might occur on a shorter timescale. Pictures of Titan were taken in seven filters on each visit: 619, 888, 902, 916, 928, 940, and 953 nm. Four of these wavelengths (902 through 940 nm) made use of the linear ramp filter (LRF), which has a 1% FWHM. The three other fixed filters have a 2% FWHM. The LRF does not acquire all wavelengths on the Planetary Camera (PC); our 890–940 nm images were obtained with one of the Wide Field Camera arrays. The LRF images thus have a plate scale of 0".1 pixel<sup>-1</sup>, equivalent to 8 or 9 pixels across Titan's equator. The three fixed filters were used with the 0".046 pixel<sup>-1</sup> resolution PC. To help offset the poorer resolution of images obtained with the LRF, we obtained pairs of images at each LRF wavelength dithered by 2.5 pixels in the *X*- and *Y*-directions on the CCD. The LRF images from visits 1, 3, and 4 were overexposed and are not used. We present haze profiles for the longitudes imaged in visits 2 and 5, centered at 217° and 242°, respectively.

Titan is small enough that the change in wavelengths passed by the LRF is insignificant over Titan's disk. The LRF wavelength shift is 0.435 Å pixel<sup>-1</sup>, or about 3.9 Å over Titan's disk. This shift is small compared with the 115 Å FWHM of the LRF.

### 2.1. Data Reduction

All images were processed through the standard *HST* WFPC2 pipeline, which includes corrections for CCD bias,

dark current, and flat-fielding. Two images contained cosmic-ray hits on Titan's disk, which we corrected by replacing the bad pixels with linearly interpolated values based on the local 3 × 3 neighborhood.

We extracted 3".2 × 3".2 subframes (6".4 × 6".4 for the LRF images) containing Titan's disk and calculated Titan's disk center in each subframe. We estimated the disk center by comparing an *HST* frame with a model-generated disk (constructed at a known location) having the same orientation, plate scale, lighting geometry (and therefore the same defect of illumination), and limb-brightening profile. We initially used the location of the cross-correlation peak as the (*X*, *Y*)-offset between the two disks, but our estimated cross-correlation peaks were typically accurate to no better than 0.25 pixels. We achieved better accuracy (better than 0.1 pixels) with a grid search, that is, by iteratively moving the model-generated image until linear fits to slices across the observed-minus-model residuals had flat slopes in the *X*- and *Y*-directions.

We found that accurate disk positions and point-spread functions were necessary when fitting the haze abundances at pixels on Titan's limb. We used Tiny Tim (version 4.4, downloaded from the STScI Web site) to generate PSFs for each image. After convolving a model-generated image with its PSF, we would also convolve it with a 3 × 3 charge dispersal kernel as recommended in the Tiny Tim documentation. It is also important to note that Titan's apparent diameter is a function of wavelength; Titan appears larger at shorter wavelengths because Titan's aerosols are better scatterers at shorter wavelengths.

The model-generated Titans require a “gain factor” that relates Titan's geometric albedo to WFPC2 pixel values. This gain factor can be calculated from the relation

$$\text{gain factor} = \frac{\text{sum of } HST \text{ pixels in Titan's disk}}{(2/3)pR^2},$$

where *p* is Titan's geometric albedo (Karkoschka 1994) in a given filter and *R* is Titan's radius in pixels (Table 2). Note that *p* and *R* have to be consistent, despite the fact that Titan's apparent size is a function of wavelength. We choose the solid surface radius (*R* = 2575 km) to be consistent with Karkoschka's calculation of Titan's albedos.

We have weighted the methane absorption coefficients by the *HST* system throughput functions to get effective CH<sub>4</sub> absorption coefficients in each *HST* filter. The system throughputs in each PC filter are documented in the WFPC2 manual (available from the STScI Web site). The LRF system throughputs are well modeled as Gaussian-

TABLE 1  
LIST OF OBSERVATIONS

Visit	Date (1996)	Sub-Earth Latitude (deg)	Sub-Earth Longitude (deg)	Subsolar Latitude (deg)	Subsolar Longitude (deg)
1.....	Oct 17	−3.78	339.79	−5.03	338.29
2.....	Oct 28	−3.50	217.46	−5.19	215.72
3.....	Oct 22	−3.65	81.58	−5.10	80.59
4.....	Oct 25	−3.57	149.51	−5.15	148.48
5.....	Oct 29	−3.47	241.98	−5.21	239.86

TABLE 2  
TITAN'S FILTER-WEIGHTED GEOMETRIC ALBEDOS AND “GAIN FACTORS”  
(FROM VISIT 2)

Wavelength (nm)	Filter-weighted Geometric Albedo	Geometric Albedo at Center λ	Gain Factor
619.....	0.226	0.222	42,421.9
888.....	0.086	0.084	52,758.4
902.....	0.117	0.100	73,532.2
916.....	0.173	0.168	44,873.7
928.....	0.231	0.233	37,168.9
940.....	0.261	0.280	30,724.5
953.....	0.195	0.204	48,133.0

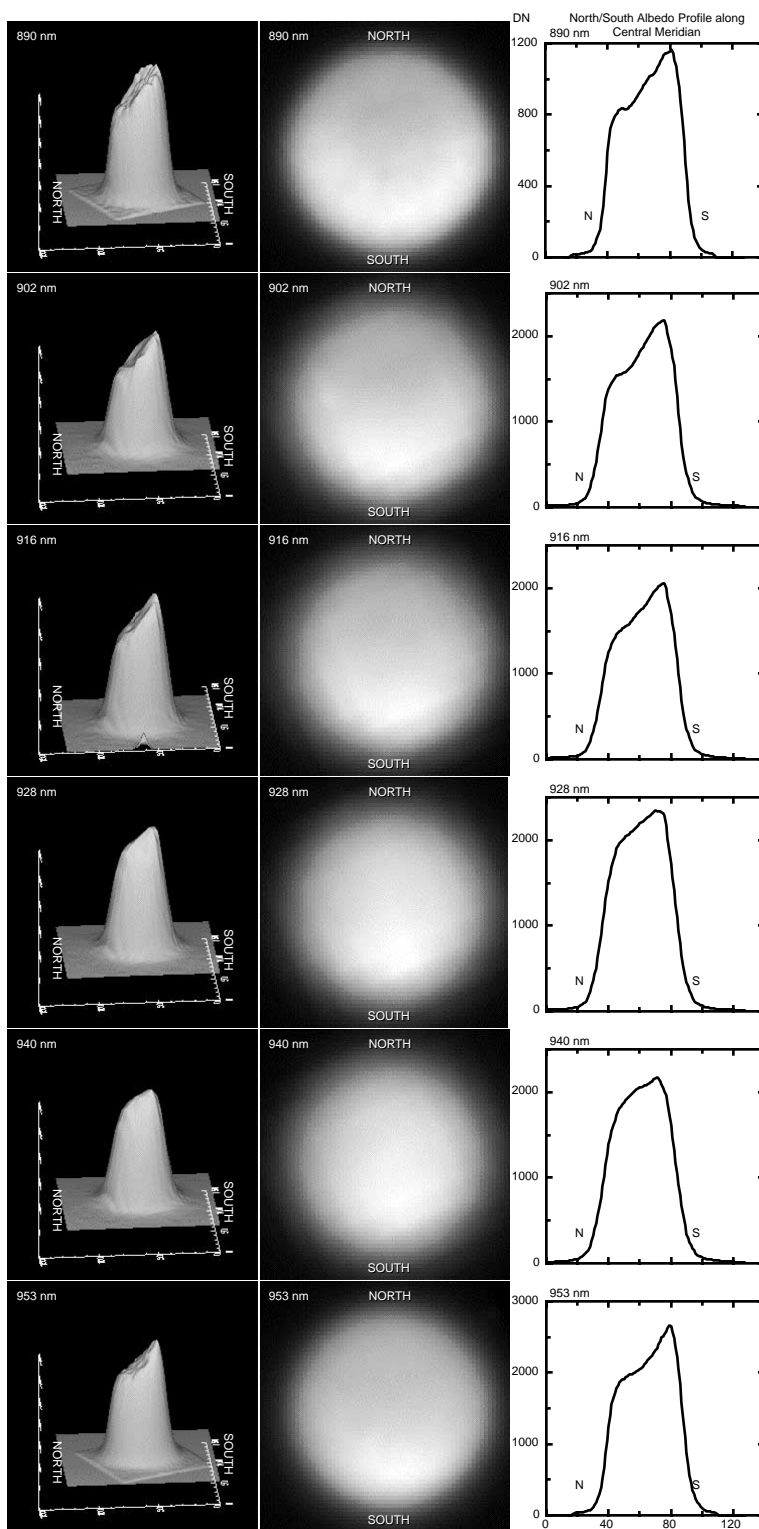


FIG. 4.—Sample of the WFPC2 observations used in this paper, arranged top to bottom in order of ascending wavelength. *Left*, relief rendering of the Titan disks; *middle*, the disks after they have been rotated and expanded to a common reference frame; *right*, Titan's brightness from north to south along the disk's central longitude, clearly showing that the south pole is brighter than the north (a result of higher concentrations of bright haze particles in the south at this Titan season) and that more limb brightening occurs in the stronger methane bands.

shaped functions. We used quadratic polynomials to model the Gaussian amplitudes, central wavelengths, and FWHM of the system throughputs in the four LRF wavelengths, based on LRF system throughputs at 50 nm intervals from Biretta, Baggett, & Noll (1996).

## 2.2. Image Gallery

Figure 4 shows a subset of the 36 images from the five visits of program 6733. In all images, the south pole is markedly brighter than the north, as expected, given the higher



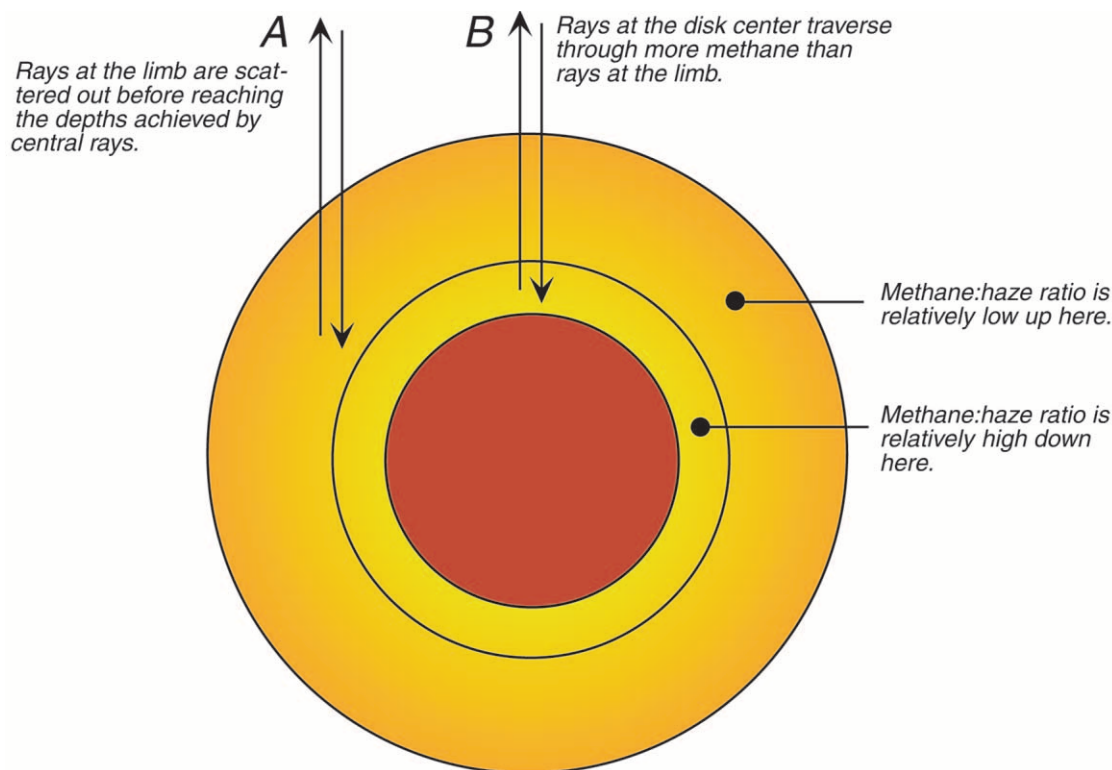


FIG. 5.—Qualitative explanation for limb brightening. The methane abundance (relative to haze) increases near the surface. As a result, photons incident at Titan's limb will likely be scattered out before they traverse through as much methane as photons that are incident at the disk center.

concentration of bright haze particles in the south. There is also limb brightening in the methane-band images, a result of the relative amounts of haze and methane as a function of altitude (Fig. 5). In theory, the limb profile might be exploited to solve for the separate vertical distributions of haze and  $\text{CH}_4$  gas, but in practice, the spatial resolution of our images was not sufficient to decouple those two abundances based on small changes to the limb profile.

### 3. ANALYSIS: DETERMINING HAZE OPTICAL DEPTHS

#### 3.1. Methane as a Vertical Discriminator

Methane's absorption coefficient is 3 orders of magnitude greater in the center of the 890 nm band than in the 940 nm window (Karkoschka 1994). Table 3 shows that the one-way single-air-mass optical depths due to methane alone are less than 0.35 in the clearest window (the LRF 940 nm

band) but over 101 in the most obscured window, the 888 nm band. Table 3 also shows how these varying optical depths translate directly to vertical resolution; at 940 nm, there is not enough optical depth due to  $\text{CH}_4$  molecules to obscure photons from the surface, but at 888 nm  $\text{CH}_4$  by itself creates a single-air-mass optical depth of 1 at an altitude of 78.7 km.

#### 3.2. Generating Model Titans

To gauge how well a given haze profile matches a set of *HST* observations, we generate synthetic Titan disks to compare against actual *HST* observations, which means that we generate synthetic Titans to match the orientation and plate scale of arbitrary *HST* images. This section describes how those disks are generated from a set of model parameters. The basic procedure is as follows:

1. Determine the Titan-centric latitudes and longitudes at each  $(x, y)$ -position on the WFPC2 CCD image, then

TABLE 3  
METHANE AS A VERTICAL DISCRIMINATOR

$\lambda$ (nm)	Filter	Absorption Coefficient <sup>a</sup>	One-Way $\tau_{\text{CH}_4}$	$\tau_{\text{CH}_4} = 1$ Alt. (km)	$\tau_{\text{N}_2}$ (Rayleigh)
619 .....	FQCH4N15-B	0.60	3.1	15.0	0.723
888 .....	FQCH4N15-D	25.26	101.2	78.7	0.169
902 .....	LRF	9.24	37.1	57.9	0.160
916 .....	LRF	0.76	3.2	19.9	0.151
928 .....	LRF	0.16	0.78	...	0.143
940 .....	LRF	0.05	0.34	...	0.136
953 .....	F953N	0.32	1.41	5.2	0.129

<sup>a</sup> Units of  $(\text{km amagat})^{-1}$ .

determine the angles between the surface normal at that point and the vectors to the observer and the Sun.

2. Determine the geometric albedo for each pixel in a given *HST* observation of Titan's disk. We use a radiative transfer (RT) code based on Toon et al. (1992). This is a two-stream plane-parallel code—admittedly a problem for pixels that lie near the limb.

3. Convert the geometric albedos into *HST* data numbers using a “gain factor” (Table 2), then convolve each synthetic disk with a model PSF generated with Tiny Tim 4. At this point, we can compare the observed and modeled Titan disks.

### 3.2.1. The Radiative Transfer Code

Our RT code divides Titan's atmosphere into 147 layers increasing in thickness from 0.5 km at the surface to 50 km at an altitude of 1200 km. For altitudes above 126 km, we use a haze extinction profile equal to that reported by Rages & Pollack (1983) at Titan's equator at the time of the *Voyager* encounters. Below 126 km we begin with an extinction profile that matches the nitrogen number density profile (as it nearly does above 150 km, according to Rages & Pollack 1983), initially scaled so that the total optical depth below 150 km is 1.0.

As an aside, our filter selection (0.62–0.95  $\mu\text{m}$ ) *cannot* resolve vertical structure above  $\sim 50$  km. In particular, we cannot monitor the evolution of the haze gap at 300–350 km that was seen in *Voyager* flyby images. One future strategy to resolve those altitudes might be to look at images taken near the ethane band around 12  $\mu\text{m}$ , since the thermal emission contribution function from Titan's atmosphere at these wavelengths does peak near 300 km.

The input parameters for the RT code are the single-scattering albedos for gas and haze particles ( $\omega_G$  and  $\omega_H$ ), the optical depths within each layer due to gas and haze ( $\tau_G$  and  $\tau_H$ ), and an asymmetry factor  $g$  for the haze scattering phase function. These five parameters can be varied from layer to layer. In addition, we set the slant path through each layer depending on the lines of sight to the observer and the Sun.

The two gas parameters ( $\omega_G$  and  $\tau_G$ ) represent the behavior of an average gas particle. We estimate  $\omega_G$  by making two simplifying assumptions: First, we assume that all of the atmospheric absorption is due to interactions with  $\text{CH}_4$  molecules, and second, we assume that all of the atmospheric scattering is due to interactions with the much more prevalent (but less optically active)  $\text{N}_2$  molecules.

The Rayleigh scattering by  $\text{N}_2$  molecules is proportional to the familiar minus-fourth power of wavelength:

$$\tau_s = 0.10625\lambda^{-4}, \quad (1)$$

where  $\tau_s$  is the total scattering optical depth by  $\text{N}_2$  molecules for a one-way trip through Titan's atmosphere, assuming the Lellouch et al. (1989) profile, and  $\lambda$  is the wavelength of light in microns. The optical depth for separate layers scales with the fractional number density of  $\text{N}_2$  molecules in that layer,

$$\tau_a = Nk, \quad (2)$$

where  $\tau_a$  is the absorption optical depth due to  $\text{CH}_4$  molecules for a layer in the atmosphere,  $N$  is the column abundance in the layer, and  $k$  is the extinction coefficient at a

particular wavelength (Table 3). The single-scattering albedo,  $\omega_G$ , is the ratio  $\tau_s/(\tau_s + \tau_a)$ .

The optical depths due to methane and haze are highly correlated; we were not able to separate these two quantities from this *HST* data set alone. In this paper we therefore assume that the methane profile is the same as specified by Lellouch et al. (1989), namely, a fractional number abundance of 1.5% throughout the atmosphere except near the surface, where the  $\text{CH}_4$  abundance rises to 8%. We do not model any latitudinal variation of  $\text{CH}_4$  profiles in this paper. We also fitted for haze abundances with an assumed  $\text{CH}_4$  surface abundance of 6% instead of 8%. The change in the total haze optical depth is nearly a linear function of the assumed methane abundance, as shown in Table 5 below.

A final input parameter to the RT code is the surface albedo. Since we cannot distinguish between the surface albedo and the abundance of haze particles just above the surface, we are forced to solve for the *combined* reflectance due to the surface and the lowest layer of aerosols. The aerosols near the surface have extremely high single-scattering albedos, which means that an error in the surface albedo translates to a change in the low-altitude haze abundance in the opposite sense (i.e., higher surface albedos are compatible with lower haze abundances). In practice, we set the surface albedo to zero, with the understanding that our low-level haze abundances might *decrease* if the surface albedo is actually higher than zero. The decrease in haze abundance that corresponds to surface albedos of 0.1 or 0.2 is not large; a mere 7% decrease in optical depth for a haze layer above a 0.2 albedo surface results in the *same* overall albedo as the original haze layer combined with a zero-albedo surface. We developed a Monte Carlo RT code to assess this relation between surface albedo and low-altitude haze abundance. We assumed bright aerosols ( $\omega_G = 0.98$ ) and a tropospheric haze layer with a nominal optical depth of 1.0, which is approximately the optical depth we find between the surface and 40 km at the equator.

To compare albedos from the various filters at a given latitude-longitude point, we co-register all of the *HST* images within each visit, which means that we rotate each image so that Titan's north pole is “up,” expand the images to a common plate scale, and translate the images to a common position. These transformed images are used in a five-parameter nonlinear least-squares fit of the aerosol extinction profile along a single latitude-longitude column (see § 3.4). We also solve for the three-dimensional distribution of haze using a second technique in which we solve for the haze profiles separately based on the brightness of individual images and then combine the results into a composite three-dimensional profile. We will refer to these two techniques as the *column method* and the *composite method*, respectively. In the composite method we use a grid spanning Titan's sphere that has 450 nodes, 15 in latitude and 30 in longitude. The longitudinal spacing between nodes is a constant  $12^\circ$ , but the latitudinal nodes are spaced so that the projected distance between nodes is constant (i.e., the nodes are more concentrated at the equator).

To interpolate between any *HST* image's pixels and the reference grid, we calculate the interpolated values as a weighted average of the three closest nodes in the destination grid. The weights of the three grid points are determined by the inverse squares of their angular distances from the point at which we require an interpolated value.

### 3.3. Fractal Modeling of Haze

We have modeled the haze particles as fractal agglomerations of spheres, as described in Rannou et al. (1997). The scattering by fractal aggregates is significantly different from scattering by spheres. We use code developed by Rannou et al. to estimate how haze aggregates grow as functions of altitude. In this model, the particles begin as single spherical monomers at 700 km in Titan's atmosphere. As they descend, they form aggregates of two, four, eight, etc., monomers. Since the scattering cross sections increase with size faster than the absorption cross sections do, the single-scattering albedos, which are dark at the highest altitudes, eventually become quite bright (Fig. 6). The factors that go into the fractal haze model include a production rate, real and imaginary indices of refraction, and an electrostatic repulsion factor. We use a set of parameters developed by P. R. based on haze profile solutions that best match Titan's spectra at IR wavelengths from 890 to 950 nm.

### 3.4. Fitting Procedure

We use two separate algorithms to extract haze optical depths. The *column method* determines the vertical extinction profile at a single latitude-longitude location. The *composite method* solves for the haze optical depths over Titan's entire projected disk by separately fitting for the haze abundances that best match individual WFPC2 images. Since each image probes a different depth, the separate disk solutions are combined into a composite three-dimensional haze distribution. The two methods are complementary. The column method is fast and provides a covariance matrix that tells us the correlations between the haze optical depths found in different layers. The composite method does not necessarily minimize the residuals between the model and all of the *HST* images, but unlike the column method, it does derive vertical haze profiles without imposing an arbitrary set of boundaries between layers, and it is less sensitive to flux from neighboring pixels contaminating the solution for a particular column. The WFPC2 point-spread func-

tions are broad enough to smear flux between adjacent columns. This is especially problematic near the limb, where the geometry of neighboring columns varies more quickly than at the disk center. For this reason, we only apply the single-column fit at disk centers, even though there is information to be mined in the center-to-limb albedo profiles within each filter. In addition, both methods currently rely on a plane-parallel two-stream RT code to translate haze profiles into WFPC2 pixel brightnesses. This code is not accurate near Titan's limb; Liou (1992) estimates that errors as high as 10%–15% occur near the limb with this type of RT code. Two improvements we hope to make in the future are to deconvolve the WFPC2 images so that the effective PSF is smaller than a pixel and to develop an RT code that accounts for the spherical geometry of Titan's atmosphere near the limb.

#### 3.4.1. The Column Method: Implementation

The column method determines the vertical haze profile at a single pixel. Five parameters represent the extinction in five layers from the surface to 126 km. The extinction is treated as a constant within a layer, as opposed to an exponential, for example. The extinction due to haze above 126 km is set to the profile reported by Rages & Pollack (1983) at Titan's equator during the *Voyager* encounters. A Marquardt-Levenberg nonlinear least-squares algorithm is used to adjust the extinction profiles in the five layers until the residuals between the WFPC2 pixel values (at the six wavelengths from 888 to 953 nm) and the RT-generated model values are minimized.

#### 3.4.2. The Column Method: Results

We present here vertical haze profiles for a five-layer fit with boundaries at 0, 16, 32, 50, 76, and 126 km. In both visits 2 and 5, there is a surprising gap at the 16–32 km layer, where the fitted extinction is less than that found in the adjacent layers (Figs. 7–8). This gap is significant in that it may be evidence of methane or ethane condensation taking place in Titan's troposphere.

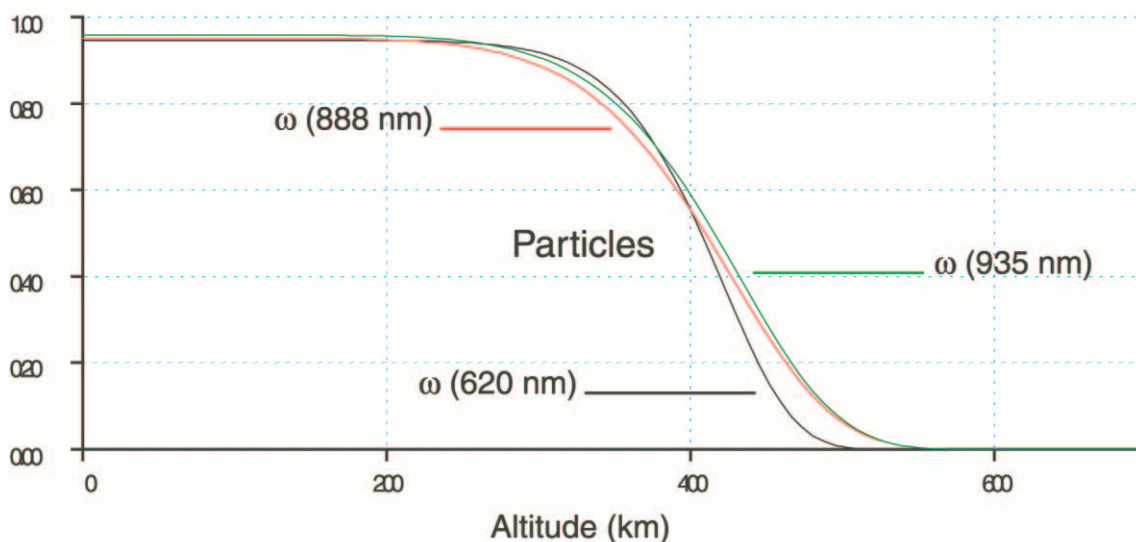


FIG. 6.—Modeled single-scattering albedo of the haze particles. We model haze particles as fractal agglomerations of spheres. The agglomerations grow bigger and more complex (more spheres) as they descend, with the main result being that their scattering cross section grows faster than their absorption cross section. Here we see that the modeled albedo increases as the haze particles descend.



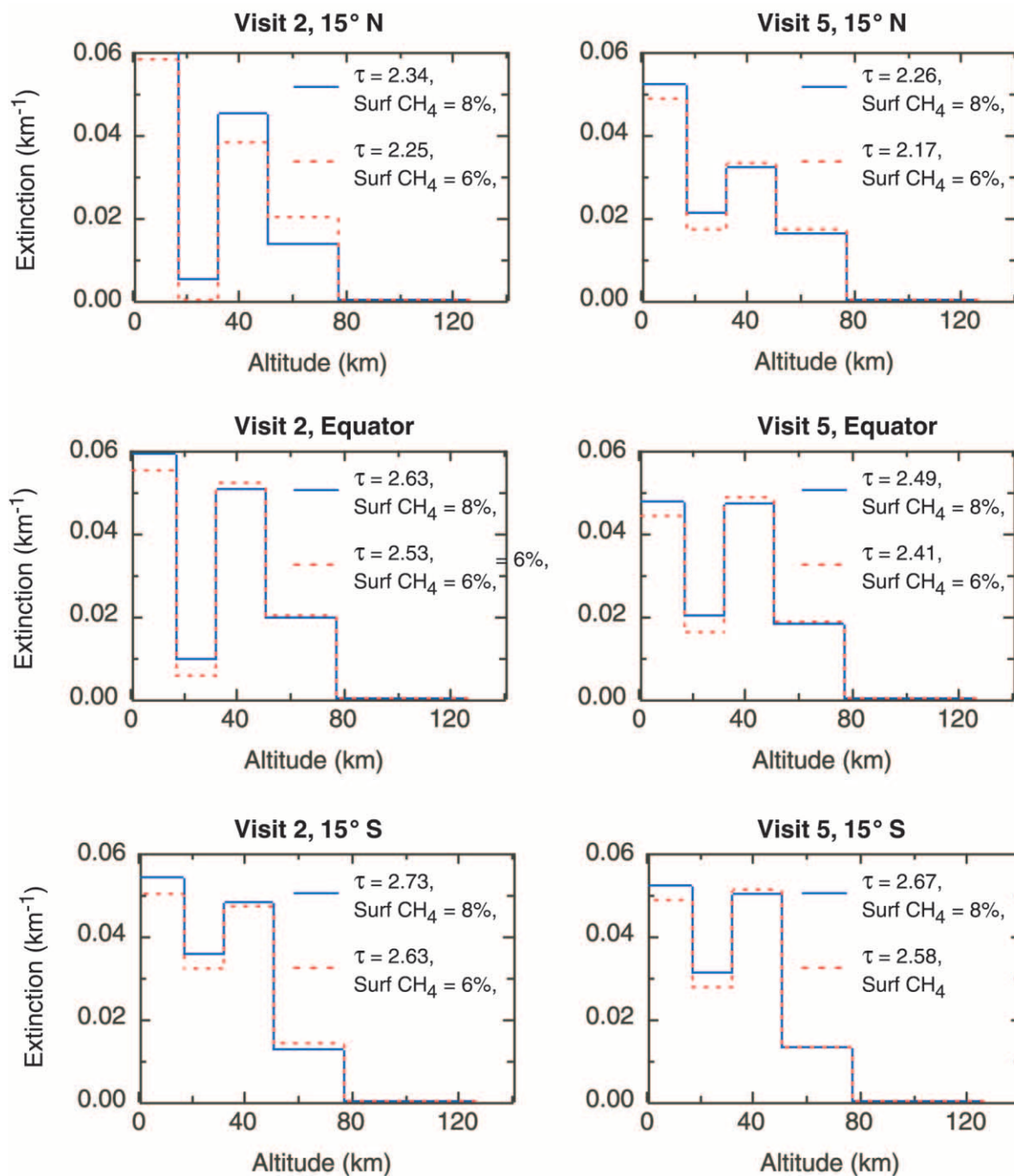


FIG. 7.—Three interesting results that come out of the column-method solution. First, there appears to be a gap in the vertical distribution of haze between 16 and 32 km (the second layer from the bottom in this fit). Second, this gap is obvious in the north but less apparent in the south. Third, the lowest-level haze bin (0–16 km) shows more haze in the north than the south, unlike every other altitude bin, where the haze is more concentrated in the south. The total one-way haze optical depths range from roughly 2 to 2.6. One possible explanation for the gap is that ethane or methane condensation onto aerosols takes place in this altitude range, increasing the aerosols' rates of descent.

Is it really possible to distinguish haze at 0–16 km from haze at 16–32 km (for example) using the *HST* Cycle 6 data set? To answer this question we perturb the haze profile at different altitudes, calculate partial derivatives of the modeled brightness as a function of the haze extinction at different altitudes, and build normalized covariance matrices from those partial derivatives. Table 4 presents normalized covariance matrices at the central meridians of visits 2 and 5 at three latitudes ( $\text{S}15^\circ$ ,  $0^\circ$ , and  $\text{N}15^\circ$ ).

We see that adjacent layers are often anticorrelated, indicating that the sum of haze opacity from two layers is constrained better than the distribution of haze between the two layers. The highest correlations occur between the 50–76 and 76–126 km layers (as we expect, since our *HST* filter set does not resolve this altitude range). We cannot determine the vertical structure above 126 km; our profiles above 126 km are the same as the assumed initial conditions. Although some of the correlation coefficients are close to 1



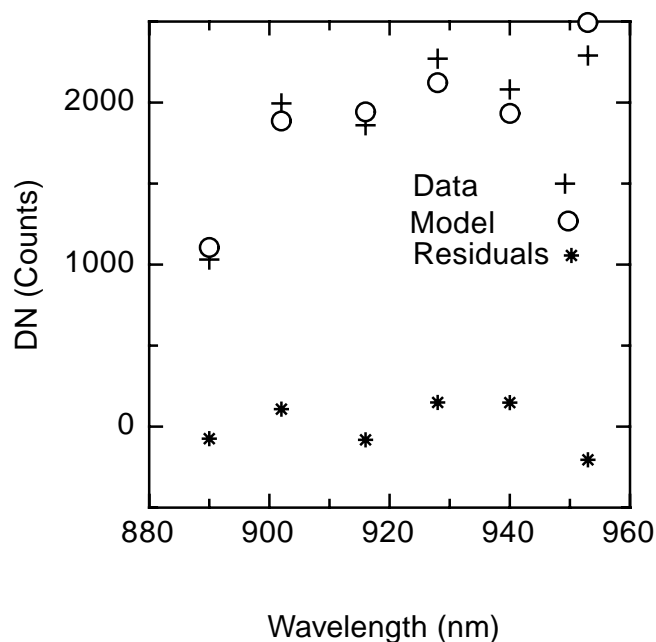


FIG. 8.—Residuals (data minus model) for the column-method best fit. They are as large as 10% of the data pixel values. This pattern of residuals (positive or negative at specific wavelengths) is repeated at every column for which we have constructed a fit near Titan's disk center in the visit-2 and visit-5 data sets. The cause of the systematic mismatches is not known, but it is not a simple function of wavelength.

(or  $-1$ ), it is important to note that the correlations between the lowest two layers are always less than 0.5 in magnitude. In other words, our *HST* filter set can distinguish between haze at 0–16 km and at 16–32 km.

How sensitive are the various filters to changes in the surface albedo? We have generated a set of synthetic Titan images in which the surface albedo has been increased from 0 to 0.4, shown in Figure 9. The 940 nm images are twice as sensitive to surface albedo variations as the 928 nm images. In passing, we note that even though the 953 nm and 940 nm filters are similar, the wider (2%) F953N filter is less than a third as sensitive to surface changes as the 1%-wide LRF 940 nm filter. Filters that cover some regions of methane absorption (as the F953N filter does) are contaminated by scattered light from above the tropopause. If surface maps are the goal, then one should employ narrowband filters centered exclusively on methane transmission windows.

How sensitive is the haze solution to the assumed methane profile? We repeated the column fits with a methane profile that increases to 6% at the surface instead of 8%. To first order, we find that a decrease in methane (an absorbing atmospheric constituent) requires a corresponding decrease in the amount of bright haze. Table 5 shows that the relation between the *assumed* CH<sub>4</sub> surface abundance and the *fitted* total haze opacities is essentially linear.

#### 3.4.3. The Composite Method: Implementation

The composite method iterates to find the vertical haze optical depth profile at every pixel. For altitudes above 126 km, we initially use an extinction profile equal to that reported by Rages & Pollack (1983) at Titan's equator at the time of the *Voyager* encounters. Below 126 km we assume that the haze extinction profile matches the atmo-

spheric number density profile (as it nearly does above 126 km).

Once an estimate of the haze profile has been assumed, it is straightforward to find the total haze optical depth that must scale the profile to match the observed *HST* pixel value. Because the haze particles are so bright, the modeled albedo generated by the RT code increases roughly in proportion to the amount of haze in the column. We take advantage of this near-linearity by evaluating modeled *HST* pixel values at five guesses for the total haze optical depth and then interpolating with a quadratic to estimate the total  $\tau_H$  that corresponds to each *HST* pixel.

If by remarkable chance we had initially hit upon the correct haze profile, the maps of total  $\tau_H$  would be identical in each filter, since each filter would just be sampling various vertical windows of the same vertical distribution. The total  $\tau_H$  maps are *not* identical, however; much more haze is required by the model to match the *HST* albedos in methane-band images than the methane-window ones. We therefore proceed to build a composite three-dimensional map of  $\tau_H$  by combining all of the haze maps determined from the separate filters. We do this on a layer-by-layer basis; the highest layers resemble the 890 nm solution, since that filter's contribution function peaks at the highest altitude (near 50 km), while the lowest layers are weighted most strongly by the 940 nm solution.

To estimate the relative weights of each filter's  $\tau_H$  map as functions of altitude, we need to know how sensitive each filter is to the intensity at any given altitude. This calls for contribution functions,

$$C(z, \mu) = J(z, \mu)W(z, \mu), \quad (3)$$

where  $J(z, \mu)$  and  $W(z, \mu)$  are the source and weighting functions at altitude  $z$  in the  $\mu$ -direction. The weighting function is the gradient of the transmittance (Hanel et al. 1992, p. 131). If we neglect the surface as a source, then the wavelength-dependent contribution functions are equivalent to the derivatives of the intensity in the  $\mu$ -direction with respect to altitude. We approximate the contribution functions with the finite differences of the upwelling intensities that are calculated by our two-stream RT code (Fig. 10). Incidentally, it is now clear why the 50–76 km layer and the 76–126 km layer extinctions are so highly correlated in the column method; since *all* of the contribution function peaks lie below 50 km, it is extremely difficult to resolve vertical haze opacity profiles above that altitude.

Once we have assembled a composite three-dimensional map of haze optical depths, we extract vertical profiles from it and use those profiles in a second iteration. This cycle (fitting a map to each filter, building a composite three-dimensional  $\tau_H$  map, and extracting new profiles) converges quickly—we see decreasing change after a few iterations, as Figure 11 illustrates.

#### 3.4.4. The Composite Method: Results

As with the column method, we find that the haze profile in Titan's troposphere differs significantly from an exponential. Figure 12 shows three vertical profiles at latitudes of N16°, the equator, and S16° from the composite method three-dimensional haze solution based on images from visit 5. The profile at a latitude of S16° shows almost no evidence of the 16–32 km gap found in the column-method solution, while the profile at the equator shows an inflection point

TABLE 4  
NORMALIZED COVARIANCE MATRICES

Layer (km)	126–76 km	76–50 km	50–32 km	32–16 km	16–0 km
Visit 2 at N15°					
126–76 .....	1.00000	0.943578	−0.643280	0.951671	−0.702438
76–50 .....	0.943578	1.00000	−0.860512	0.999641	−0.437390
50–32 .....	−0.643280	−0.860512	1.00000	−0.847174	−0.0707133
32–16 .....	0.951671	0.999641	−0.847174	1.00000	−0.461142
16–0 .....	−0.702438	−0.437390	−0.0707133	−0.461142	1.00000
Visit 2 at the Equator					
126–76 .....	1.00000	0.910869	−0.486125	−0.908723	−0.407432
76–50 .....	0.910869	1.00000	−0.803440	−0.999971	0.00574836
50–32 .....	−0.486125	−0.803440	1.00000	0.806445	−0.599988
32–16 .....	−0.908723	−0.999971	0.806445	1.00000	−0.0108348
16–0 .....	−0.407432	0.00574836	−0.599988	−0.0108348	1.00000
Visit 2 at S15°					
126–76 .....	1.00000	0.896040	−0.426131	0.961417	−0.558636
76–50 .....	0.896040	1.00000	−0.783416	0.982971	−0.191475
50–32 .....	−0.426131	−0.783416	1.00000	−0.656798	−0.398275
32–16 .....	0.961417	0.982971	−0.656798	1.00000	−0.358431
16–0 .....	−0.558636	−0.191475	−0.398275	−0.358431	1.00000
Visit 5 at N15°					
126–76 .....	1.00000	0.975036	−0.833601	0.988791	0.608483
76–50 .....	0.975036	1.00000	−0.935431	0.997177	0.429781
50–32 .....	−0.833601	−0.935431	1.00000	−0.906438	−0.0984305
32–16 .....	0.988791	0.997177	−0.906438	1.00000	0.494949
16–0 .....	0.608483	0.429781	−0.0984305	0.494949	1.00000
Visit 5 at the Equator					
126–76 .....	1.00000	0.995200	−0.969484	0.997316	−0.538244
76–50 .....	0.995200	1.00000	−0.988818	0.999664	−0.464335
50–32 .....	−0.969484	−0.988818	1.00000	−0.984723	0.341338
32–16 .....	0.997316	0.999664	−0.984723	1.00000	−0.486339
16–0 .....	−0.538244	−0.464335	0.341338	−0.486339	1.00000
Visit 5 at S15°					
126–76 .....	1.00000	0.930743	−0.600336	0.970369	−0.526496
76–50 .....	0.930743	1.00000	−0.851180	0.991280	−0.209144
50–32 .....	−0.600336	−0.851180	1.00000	−0.775058	−0.301808
32–16 .....	0.970369	0.991280	−0.775058	1.00000	−0.331920
16–0 .....	−0.526496	−0.209144	−0.301808	−0.331920	1.00000

around 30–40 km. The profile at N16° shows an even more pronounced inflection point.

Clearly, the composite method is not able to fit large-amplitude structure in the vertical profiles. Nevertheless, the column method and the composite method results agree on several points:

1. The total haze optical depth decreases monotonically as the latitude varies from south to north.

2. The column method solves for haze optical depths between Titan's surface and 126 km. The total haze optical depth within that range is similar in both the column-method and composite-method solutions, although the composite-method values for  $\tau_H$  are consistently higher. In visit 2, for example, at latitudes S16°, 0°, and N16°, the composite solutions for  $\tau_H$  between 0 and 126 km at the subsolar longitude are 3.53, 3.06, and 2.84, respectively, compared with 2.73, 2.63, and 2.34 for the column method (assuming

atmospheric concentrations of CH<sub>4</sub> of 8% at the surface). The column-method totals are preferable to the composite-method values, since the composite method does not explicitly seek to minimize residuals.

3. The gap in haze optical depth found in the column method is greatest in the north and less in the south. While the gap shows up as an inflection point in the composite solution, the effect is also strongest in the north.

4. In the lower half of the troposphere, the haze optical depth is higher in the north than at the equator, unlike the haze distribution at any other altitude. This result is common to the column and composite methods.

The total optical depth due to haze is  $\sim 1.7$  over the north pole, increasing to  $\sim 2.9$  over the south pole. These values are based on column-method solutions near the poles, admittedly suspect because of our RT code's deficiencies near the limb. The column-method total haze optical depths

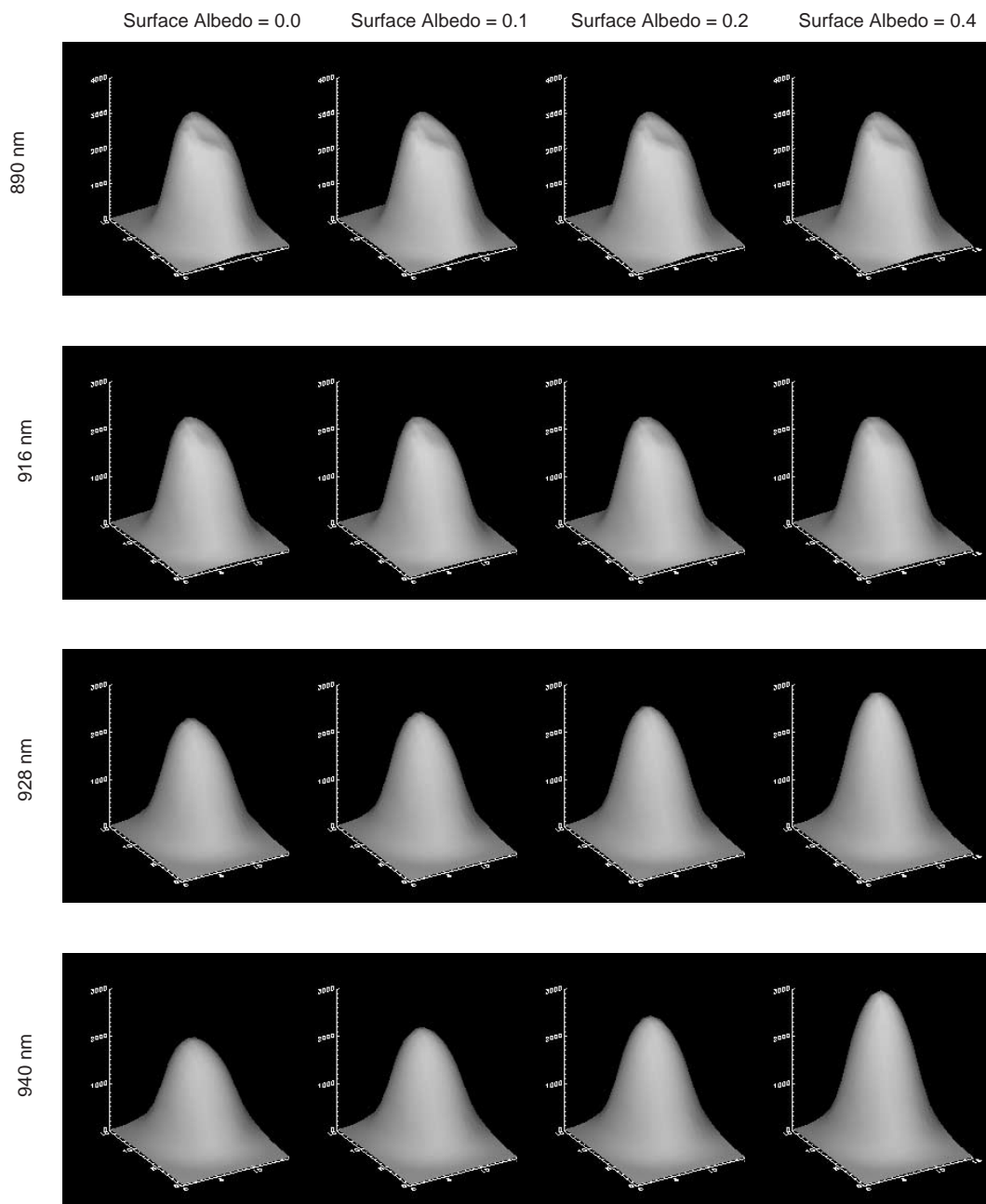


FIG. 9.—Synthetic Titan images. Each row plots four simulated Titans, assuming a model atmosphere from the composite solution, with surface albedos increasing left to right from 0 to 0.4. The wavelengths increase from top to bottom, from 890 nm [with an effective absorption coefficient of  $25.2 \text{ (km amagat)}^{-1}$ ] to 940 nm [absorption coefficient of  $0.05 \text{ (km amagat)}^{-1}$ ]. At 890 nm and even 916 nm, the changes in the surface albedo are undetectable. At 928 nm, a 0.1 change in the surface albedo produces a 6% change in the overall albedo at disk center. The 940 nm filter is almost twice as sensitive—a 0.1 change in surface albedo results in a 12% change in overall albedo at disk center.

at  $N15^\circ$  and  $S15^\circ$  are 2.26 and 2.73, respectively. One surprise is the structure in the  $\tau_H$  field at low altitudes. Figures 12 and 13 show that the low-lying haze distribution (between 0 and 16 km) has a slight buildup of haze in the north compared with the distributions at higher altitudes. The low-altitude northern haze concentration is obtained from both the visit-2 and visit-5 image series.

#### 4. DISCUSSION

*The tropospheric haze gap.*—The extinction profiles of Rages & Pollack (1983; probing down to about 125 km)

show the haze extinction to approximate an exponential, which means that the haze is, to first order, evenly mixed with the atmosphere at these higher altitudes. The haze does not remain evenly mixed down to the surface. Below  $\sim 40$  km the haze optical depth actually decreases instead of increasing in parallel with the gas abundance. What could cause the haze optical depth to decrease at these lower altitudes? Several possibilities come to mind.

First, there may be two separate haze populations in Titan's atmosphere, one of which is produced below the tropopause. We think this unlikely, because such a population would likely be composed of condensed grains, which would

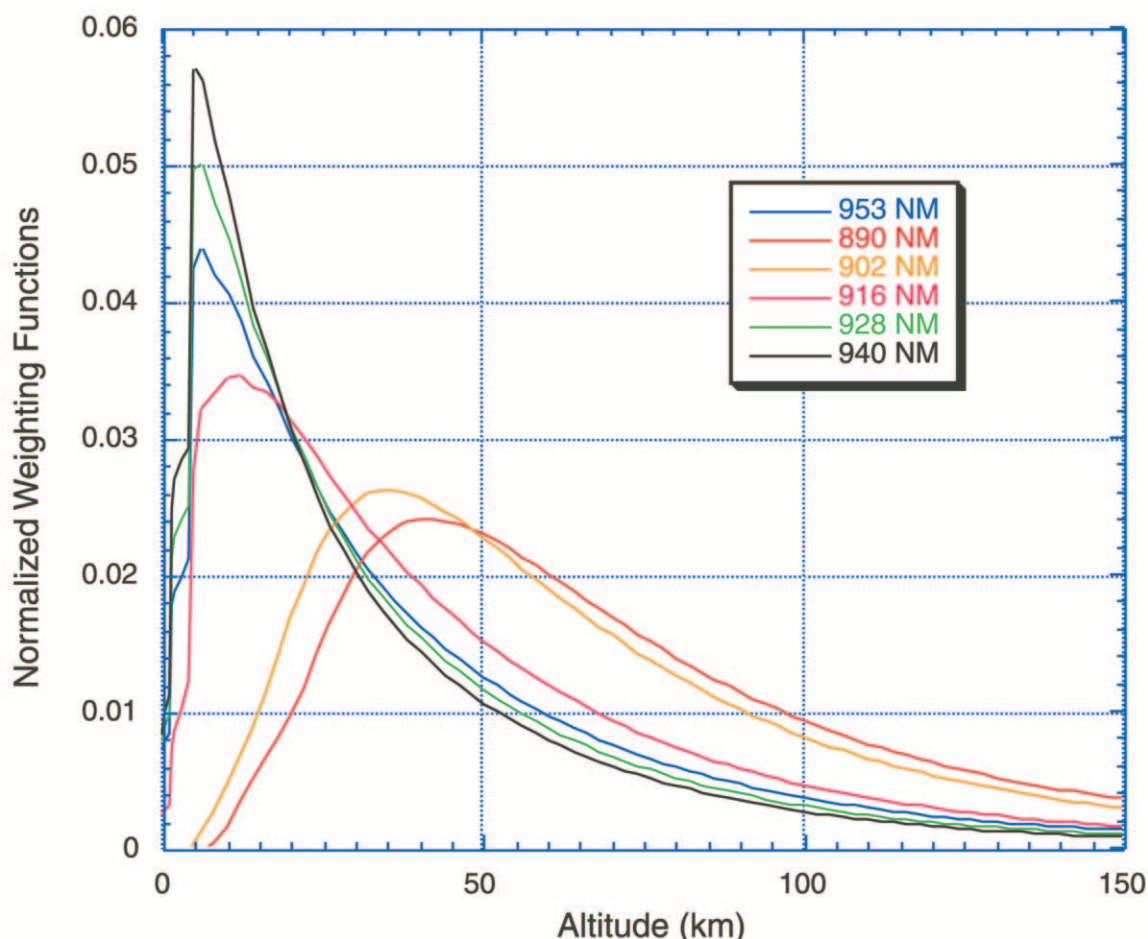


FIG. 10.—Contribution functions for all six wavelengths after 25 iterations

be large compared with  $2\ \mu\text{m}$ . Gibbard et al. (1999) have mapped Titan's surface at  $2\ \mu\text{m}$ , and they do not see evidence for a haze composed of large grains. In other words, because the one-way optical depth is so much less at  $2\ \mu\text{m}$  than at  $0.94\ \mu\text{m}$ , we believe that a second population of large aerosols does not exist.

More likely is that the known aerosol population undergoes a change as it descends. Some condensation by ethane may occur at 60 km, causing the haze particles to fall more quickly. The volatile covering might evaporate at lower altitudes, at which point the aerosols would descend more slowly. The result would be a less dense region in the altitudes of quickest descent.

*Compatibility with the thermal profile.*—The gap in the haze is not inconsistent with the thermal structure of

TABLE 5  
HAZE OPTICAL DEPTHS VERSUS ASSUMED  
CONCENTRATIONS OF METHANE  
NEAR SURFACE

Surface CH <sub>4</sub> Abundance	$\tau_{\text{total}}(\text{N}15^\circ)$	$\tau_{\text{total}}(\text{S}15^\circ)$
8% .....	2.26	2.67
7% .....	2.21	2.63
6% .....	2.17	2.58

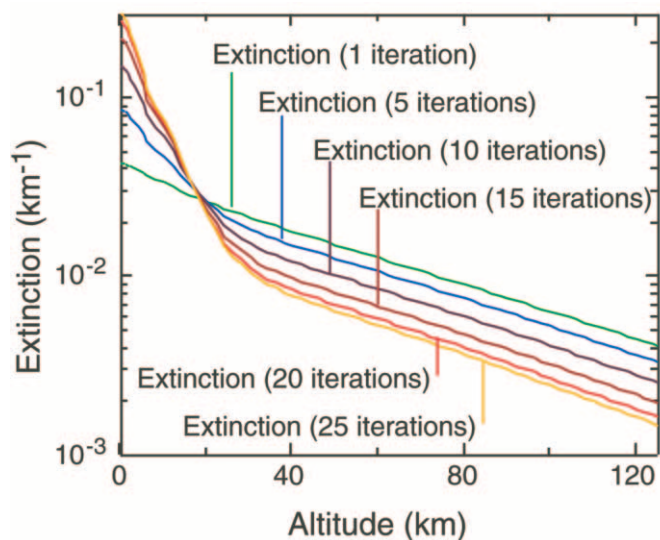


FIG. 11.—Vertical extinction profiles after one to 25 iterations. The initial profile is close to an exponential—actually a profile that assumes a constant aerosol mixing ratio with the gas at all altitudes. The composite method iterates until little change is seen in the extinction profile. Note the small variation in the profile from 20 to 25 iterations.



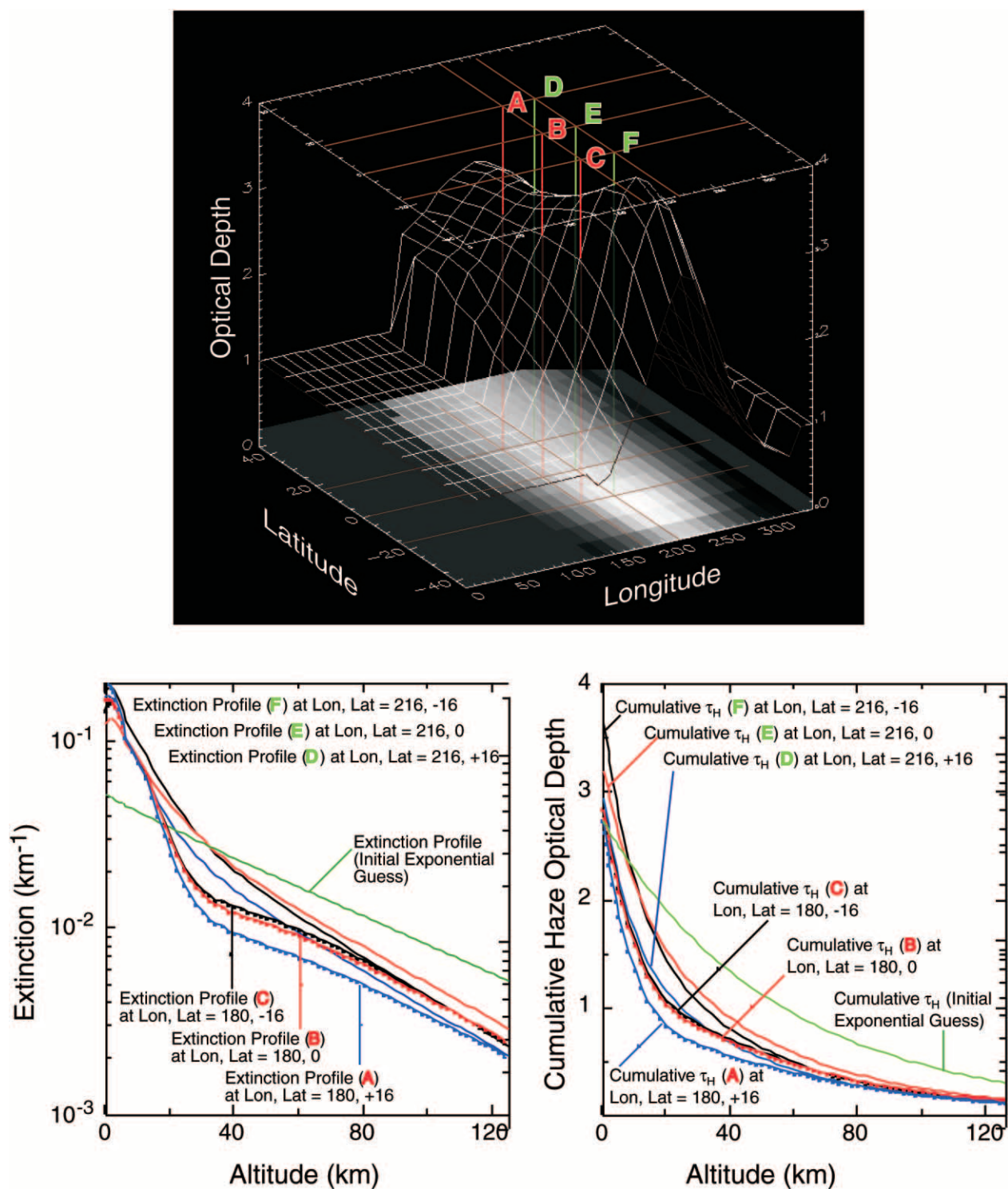


FIG. 12.—*Top*: Six locations at which we plot extinction profiles (*bottom*), superimposed on a wire-frame outline of the total one-way haze optical depths. This plot spans all  $360^\circ$  in longitude, even though we clearly have coverage over just half that range. The basic concentration of haze over the southern hemisphere is apparent. The columns at longitude  $180^\circ$  (red) show lower one-way optical depths than columns at  $216^\circ$  (green), which is nearly the subsolar meridian of visit 2. The lower optical depths on either side of the subsolar longitudes is an artifact of our plane-parallel two-stream RT code. *Bottom left*: Vertical profiles from the composite solution. Although these are much smoother than the column solution profiles, they do show an inflection near 30 km that is consistent with the gap found in the column solutions. The composite solutions also show the suggestive gap in the north, not the south. It is also noteworthy that the extinction profiles all place more haze in the troposphere than our initial estimate of a nearly exponential profile in which haze is evenly mixed with the atmosphere. *Bottom right*: Cumulative haze optical depths (measured from the top down) at the six latitude-longitude locations.

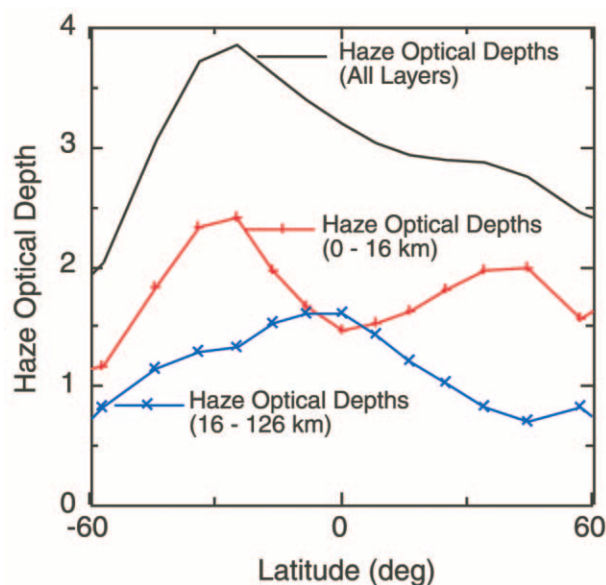


FIG. 13.—Local concentration of haze in the north at the lowest altitudes, shown in north-south traces along a central meridian.

Titan's troposphere. The stratospheric haze plays a key role in the thermal structure by causing an anti-greenhouse effect (McKay, Pollack, & Courtin 1991), but the gap located at 16–32 km is well below the altitude where this would matter.

In the troposphere, the IR absorption is completely dominated by the collision-induced opacity of  $N_2$ ,  $CH_4$ , and to a lesser extent  $H_2$ . The IR absorption of the haze in the troposphere is negligible in comparison; hence, the thermal pro-

file from the *Voyager* radio occultation experiment does not rule out the haze distribution we present here.

The tropospheric haze *does* absorb solar radiation in the visible, and a gap in the haze profile will affect this absorption. However, because of the high IR opacity in the troposphere, the temperature profile in the troposphere is determined by IR exchange (the greenhouse effect) and not by the precise altitude of solar energy deposition (although the *total* amount of energy deposited does matter). If the haze were completely removed below 35 km, the change in the thermal structure would be less than 3 K throughout the troposphere.

*Low-altitude haze buildup in northern latitudes.*—A separate result is the apparent upturn in haze concentration between 0 and 16 km above the northern latitudes relative to higher altitudes. This brightening may be due to a bright surface at northern latitudes, but 2.0  $\mu m$  maps of Titan's surface do not show any such feature. Water frost does have an absorption feature in the 2  $\mu m$  methane window, so it is conceivable that a north polar  $H_2O$  frost cap exists that is bright at 0.94  $\mu m$  but dark at 2  $\mu m$ .

This haze buildup is in contrast to the monotonic north-south slope in haze abundance at all higher altitudes. It will be interesting to watch this local anomaly in the years preceding the *Cassini* encounter to see how it evolves in the context of Titan's global haze migration.

Support for proposal 6733 was provided by NASA through a grant from the Space Telescope Science Institute, which is operated by the Association of Universities for Research in Astronomy, Inc., under NASA contract NAS 5-26555. This work was also supported by an internal research grant from Southwest Research Institute.

#### REFERENCES

- Biretta, J., Baggett, S., & Noll, K. 1996, Photometric Calibration of WFPC2 Linear Ramp Filter Data in SYNPHOT (WFPC2 Instrum. Sci. Rep. 96-06) (Baltimore: STScI)
- Gibbard, S. G., Macintosh, B., Gavel, D., Max, C. E., de Pater, I., Ghez, A. M., Young, E. F., & McKay, C. P. 1999, *Icarus*, 139, 189
- Griffith, C. A., Owen, T., Miller, G. A., & Geballe, T. 1998, *Nature*, 395, 575
- Hanel, R. A., Conrath, B. J., Jennings, D. E., & Samuelson, R. E. 1992, *Exploration of the Solar System by Infrared Remote Sensing* (Cambridge: Cambridge Univ. Press)
- Karkoschka, E. 1994, *Icarus*, 111, 174
- Karkoschka, E., & Lorenz, R. D. 1997, *Icarus*, 125, 369
- Khare, B. N., Sagan, C., Arakawa, E. T., Suits, F., Callcott, T. A., & Williams, M. W. 1984, *Icarus*, 60, 127
- Lellouch, E., Coustenis, A., Gautier, D., Raulin, F., Dubouloz, N., & Frère, C. 1989, *Icarus*, 79, 328
- Lindal, G. F., Wood, G. E., Hotz, H. B., Sweetnam, D. N., Eshleman, V. R., & Tyler, G. L. 1983, *Icarus*, 53, 348
- Liou, K.-N. 1992, *Radiation and Cloud Processes in the Atmosphere* (New York: Oxford Univ. Press)
- Lorenz, R. D., Lemmon, M. T., Smith, P. H., & Lockwood, G. W. 1999, *Icarus*, 142, 391
- McKay, C. P., Martin, S. C., Griffith, C. A., & Keller, R. M. 1997, *Icarus*, 129, 498
- McKay, C. P., Pollack, J. B., & Courtin, R. 1991, *Science*, 253, 1118
- Rannou, P., Cabane, M., Botet, R., & Chassefière, E. 1997, *J. Geophys. Res.*, 102, 10997
- Rages, K., & Pollack, J. B. 1980, *Icarus*, 41, 119
- , 1983, *Icarus*, 55, 50
- Rages, K., Pollack, J. B., & Smith, P. H. 1983, *J. Geophys. Res.*, 88, 8721
- Tomasko, M. G. 1980, *J. Geophys. Res.*, 85, 5937
- Toon, O. B., McKay, C. P., Griffith, C. A., & Turco, R. P. 1992, *Icarus*, 95, 24
- West, R. A., & Smith, P. H. 1991, *Icarus*, 90, 330